ELSEVIER

Journal of Structural Geology 27 (2005) 179–197

JOURNAL OF STRUCTURAL GEOLOGY

www.elsevier.com/locate/jsg

The relationship between magmatic tiling, fluid flow and crystal fraction

Kieran F. Mulchrone[a,*], Suzanne Grogan[b], Prithwijit De[c]

[a]*Department of Applied Mathematics, National University of Ireland, Cork, Republic of Ireland*
[b]*Department of Geology, National University of Ireland, Cork, Republic of Ireland*
[c]*Department of Statistics, National University of Ireland, Cork, Republic of Ireland*

Received 21 June 2004; received in revised form 29 September 2004; accepted 20 October 2004
Available online 6 January 2005

Abstract

Tiling of crystals in magmatic rocks is used to indicate flow in the magmatic state and also as an indicator of shear sense. The status of tiling as a kinematic indicator is often regarded with caution due to a poor understanding of the dynamics involved in its development. By considering a simple numerical model involving both rotation and translation of pairs of crystal objects under different homogeneous steady state flow conditions (i.e. $0 \leq W_k \leq 1.5$), the dynamics of crystal tiling is studied in detail. A consistent relationship between tiling proportions (i.e. dextral versus sinistral) and W_k is observed. For pure shear the relationship is 50/50 whereas for simple shear one sense dominates accounting for 70% of the tiling. A similar relationship is observed for low and high crystal fractions and a wide variety of object aspect ratios. Through application of the statistics of proportions it is shown that approximately 60 observations are required for a shear sense determination, whereas for accurate estimation of W_k at least 200 observations are required. The density of tiling varies with crystal fraction and it may be possible to use the frequency of occurrence of tiling to estimate the crystal fraction at the time of tiling. It is concluded that a few observations of crystal tiling is a highly unreliable shear sense indicator.

Keywords: Kinematic vorticity number; Magmatic tiling; Statistics

1. Introduction

Magmatic tiling has long been acknowledged as a useful tool in the recognition of the occurrence of magmatic flow within igneous rocks and more importantly as a kinematic indicator for shear sense within magmatic state fabrics (Den Tex, 1969; Blumenfeld and Bouchez, 1988). Tiling of crystals involves the interaction of early-formed crystals in a viscous magma due to movements in the magma (i.e. fluid flow or deformation), which causes crystals to be rotated and translated. It has been proposed that the sense of shear of magmatic flow can then be determined from the dominant sense of rotation of the crystal tilings (Blumenfeld and Bouchez, 1988). Sense of tiling and synthetic versus antithetic tiling are illustrated in Fig. 1. Flow in magma can be conceptually subdivided into (1) a component due to magma ascent and emplacement (i.e. largely due to buoyancy forces in the magma) referred to here as internal flow and (2) a component due to tectonic movements of the surrounding rock mass referred to here as external flow. In general, a combination of internal and external flow is present (see, for example, Correa-Gomes et al., 2001). Distinguishing whether flow is dominantly of internal or external origin is of utmost importance when investigating the geological history of an igneous body.

Magmatic state fabrics such as tiling occur before the RCMP (rheological critical melt percentage; Arzi, 1978) of a magma is reached, i.e. a point where a magma transforms from a liquid (Newtonian behaviour) to a solid (non-Newtonian behaviour). This transition corresponds to 20–40% melt in granitoid magmatic systems (Arzi, 1978). Therefore, as the population density of crystals (i.e. crystal fraction) increases the likelihood of mechanical interaction between free moving crystals also increases with progressive crystallisation during dynamic magmatic flow. However, this does not preclude interaction and the occurrence

* Corresponding author. Tel.: +353-21-4903411; fax: +353-21-4270813
E-mail address: k.mulchrone@ucc.ie (K.F. Mulchrone).

0191-8141/$ - see front matter © 2005 Elsevier Ltd. All rights reserved.
doi:10.1016/j.jsg.2004.10.007

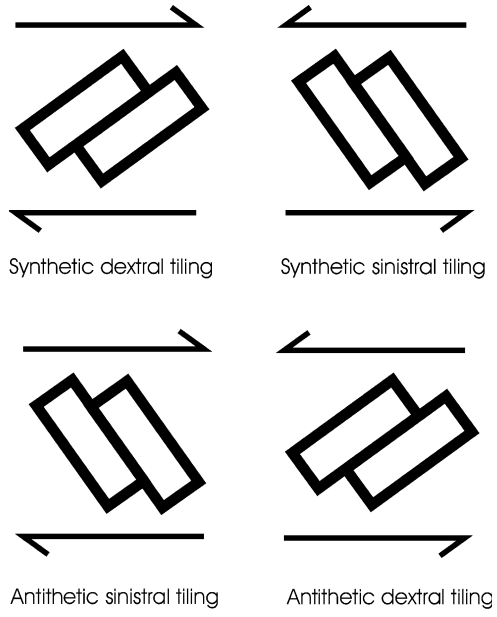

Fig. 1. Diagram of dextral and sinistral tiling and the notion of synthetic and antithetic tiling.

of magmatic tiling at an even earlier stage with a lower crystal fraction in the melt. Work by Bryon et al. (1994) on textural development during crystallisation of granitoid magmas found that at $\approx 50\%$ melt a crystal framework would develop with subsequent crystallisation in pore spaces. This would inhibit magmatic flow and magmatic fabric development. A theory shared by Arbaret et al. (1996) proposing that fabrics in magmas could form at even $>50\%$ melt fraction.

Experimental modelling of magmatic fabrics such as tiling (Fernandez et al., 1983; Arbaret et al., 1996; Correa-Gomes et al., 2001) in sheet-like bodies demonstrates that symmetric or asymmetric fabrics may develop, which is related to internal or external flow, respectively. Correa-Gomes et al. (2001) developed a model based on the PDO (preferred dimension orientation) of crystals occurring in vertical dykes or sheet-like igneous bodies with shear movement along the walls. This model uses a fabric ellipsoid as a kinematic strain marker, which is representative of crystals or xenoliths within the dyke. Through the application of different stresses along the walls of the dyke and changing magma velocities within, the development of fabrics was monitored and was predominantly found to be asymmetric in nature, especially when an external stress was applied. It is due to a concordance between this asymmetry and sense of magmatic tiling that they suggest that magmatic tiling may enable determination of a kinematic direction. However, in the above model and in previous models the reliability of using tiling as a shear indicator was always questioned as it was found that within igneous bodies the tiled phenocrysts often indicated opposing senses of shear.

Blumenfeld and Bouchez (1988) while working on the Barbey–Seroux granitoid body in France found that even though the tiled phenocrysts did show an opposing shear sense the greater percentage of them were concurrent with the overall tectonic history of the area. It remains, however, that up to 30% of tiled phenocryst pairs indicated an opposing shear sense. Therefore the "reliability of this structure is still uncertain", as stated by Passchier and Trouw (1996, p. 127). It is common practice to deduce shear sense based on a few observations of tiling sense and in effect tiling is used as a kinematic indicator. This may ultimately lead to anomalous results. It is of geological importance to understand the formation of magmatic tiling and the extent to which it may be used as a kinematic indicator. In addition, it also gives an insight into understanding the dynamics of magmatic flow and the formation of magmatic state fabrics. The model presented here for the development of tiling attempts to address the uncertainty surrounding this structure by resolving the extent to which it may be used as a kinematic indicator and formulating guidelines for understanding its significance.

2. Flow kinematics

The kinematics of deformation is described using basic concepts from continuum mechanics. For geological materials modelled as fluids, this means describing the velocity field. At certain scales most observed geological deformation is heterogeneous, but usually an alternative scale can be chosen whereby deformation can be effectively considered to be homogeneous. This greatly simplifies the mathematical description of deformation and flow (Passchier, 1997); however, it is always important to remember that this is just an approximation. An additional simplification of steady state flow is usually made in geological applications thereby eliminating any variation of the velocity field over time. Under these assumptions, the velocity field ($\mathbf{v}$) can be described in terms of the velocity gradient tensor ($\mathbf{L}$) and position ($\mathbf{x}$):

$$\mathbf{v} = \mathbf{L}\mathbf{x} \tag{1}$$

where

$$\mathbf{L} = \frac{\partial \mathbf{v}}{\partial \mathbf{x}} \tag{2}$$

and homogeneity is guaranteed here by the assumption of a linear relationship between velocity and position and also that the velocity gradient tensor is constant. It is also implicit in these relationships that the velocity at the origin is zero and the velocity gradient tensor is evaluated at the origin (and hence must be constant).

In terms of components:

$$v_i = L_{ij}x_j \tag{3}$$

$$L_{ij} = \frac{\partial v_i}{\partial x_j} \tag{4}$$

and isochoric flow implies that $L_{ii}=0$. It is convenient to consider flows described by the following velocity gradient tensor:

$$\mathbf{L} = \begin{pmatrix} 0 & L_{12} \\ L_{21} & 0 \end{pmatrix} \tag{5}$$

which automatically satisfy the isochoric assumption. The kinematical vorticity number (W_k) is given by (Ghosh, 1987):

$$W_k = \frac{L_{12} - L_{21}}{|L_{12} + L_{21}|} \tag{6}$$

By simple analysis it is clear that the general deformation under consideration encompasses the three deformation histories of Means et al. (1980) and the five steady progressive deformation categories of Ghosh (1987).

The convention for angles and rotations used here is that the positive ordinate axis is the zero angle direction and that counter-clockwise angles and rotations are positive and vice versa for the clockwise case. The eigenvectors of **L** (also known as the flow apophyses by Ramberg (1975)) are directions of zero rotation, i.e. material particles initially within these directions remain so, whereas other particles tend to be repelled from or asymptotically attracted into the flow apophyses (Passchier, 1997). They are particularly helpful in visualising the passive behaviour of points and lines as they divide the flow into zones of counter-clockwise and clockwise rotation (see Fig. 2). The eigenvectors are given by:

$$l_1 = \begin{pmatrix} \sqrt{\dfrac{L_{12}}{L_{21}}} \\ 1 \end{pmatrix} \tag{7}$$

$$l_2 = \begin{pmatrix} -\sqrt{\dfrac{L_{12}}{L_{21}}} \\ 1 \end{pmatrix} \tag{8}$$

It is clear that for $|W_k| > 1$, some of the components of the eigenvectors are imaginary and do not have a physical meaning. The two eigenvectors coincide under simple shear ($|W_k| = 1$) and in all other cases remain distinct.

3. Modelling rotation of rigid phenocrysts

Phenocrysts have been modelled in the past as rigid ellipsoids immersed in a slow-moving linear viscous (Newtonian) fluid and the hydrodynamical model of Jeffery's (1922) applied. In this paper only the 2D case is considered and the 2D version of Jeffery's (1922) model is used whereby phenocrysts are modelled as ellipses. Ghosh and Ramberg (1976) studied the characteristics of this model in detail. Quoting Jeffery (1922), Ghosh and Ramberg (1976) stated that the rotation rate ($\dot{\phi}$) of a rigid ellipse major axis during simple shear deformation is a

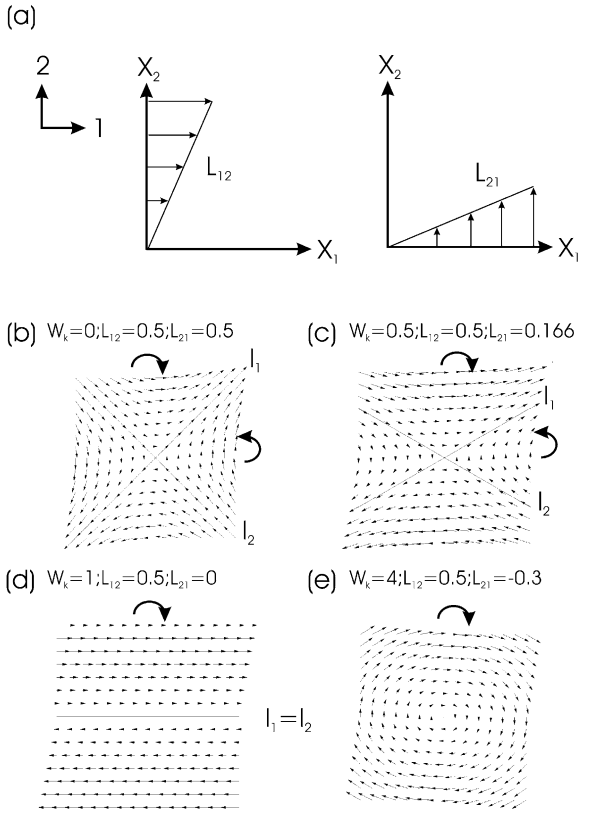

Fig. 2. (a) Velocity gradient tensor components L_{12} and L_{21} describe how the velocity vectors (small arrows) linearly vary near the origin. Combining these components in different proportions generates all possible flow types. For example, (b) $W_k=0$, pure shear with two mutually normal flow apophyses (l_1 and l_2). Heavy arrows show the local rotation sense. (c) $W_k=0.5$, intermediate between pure and simple shear, with two sub-normal flow apophyses. (d) $W_k=1$, simple shear both flow apophyses coincide along the shear direction and (e) $W_k=4$, no real apophyses exist and pulsating strain histories occur.

function of axis orientation (ϕ), shear strain rate ($\dot{\gamma}$) and ellipse axial ratio (R) as follows:

$$\dot{\phi} = \frac{\dot{\gamma}(R^2\cos^2\phi + \sin^2\phi)}{R^2 + 1} \tag{9}$$

however, they use the convention that the positive coordinate axis is the zero orientation and that clockwise rotation is positive. In order to conform with the kinematics of the general flow described earlier (see Eq. (5)), this equation must be modified. For the general deformation considered here, rate of rotation of the rigid ellipse long axis is derived to be:

$$\dot{\phi} = \frac{L_{21} - L_{12}}{2} + \frac{(L_{21} + L_{12})(R^2 - 1)}{2(R^2 + 1)}\cos 2\phi \tag{10}$$

This is an interesting equation in itself and can be used to reproduce the results of Ghosh and Ramberg (1976); however, in addition, flows with $|W_k| > 1$, i.e. pulsating strain histories, can also be studied.

A complete understanding of the solution of Eq. (10) is possible without solving it by employing some of the

techniques of non-linear dynamics. Much of this analysis can be performed graphically as well as symbolically, thus an intuitive understanding is possible for non-mathematicians. First the equation is rearranged so that it is written in terms of W_k (using Eq. (6)):

$$\dot{\phi} = \frac{L_{21} + L_{12}}{2}\left(-W_k + \frac{(R^2-1)}{(R^2+1)}\cos 2\phi\right) \tag{11}$$

providing $L_{21}+L_{12}>0$ otherwise the sign of W_k term should change. This requirement is ensured by choosing $L_{12}>0$ and $L_{21}>-L_{12}$ giving $W_k>-1$. Eq. (11) can also be written as:

$$\dot{\phi} = A + B\cos 2\phi \tag{12}$$

where $A=-(W_k(L_{21}+L_{12})/2)$ and $B=(L_{21}+L_{12})(R^2-1)/2(R^2+1)$. This is an equation that occurs commonly in many other branches of science and engineering (Strogatz, 1994) and is termed a non-uniform oscillator. Eq. (12) emerges from Jeffery's (1922) solution and has been studied by Ghosh and Ramberg (1976), Freeman (1985), Passchier (1987) and Jezek et al. (1996), as well as many others in the context of structural geology. It has period π, so that the full characteristics of the equation can be examined for ϕ in $[-\pi/2, \pi/2]$. Taking W_k as being in the interval $[-1, \infty]$ (so that Eq. (11) is valid), there are five distinct behaviours depending on the ratio $A/B=-(W_k(R^2+1)/(R^2-1))$ (see Fig. 3):

1. $A/B<-1$: in this case there are no fixed points (orientations were the rotation rate is zero) and all objects rotate with the same sense.
2. $A/B=-1$: a single fixed point has emerged and all objects rotate in the same sense; however, objects whose long axis is parallel to the fixed point do not rotate. This fixed point is termed half-stable insofar as on one side objects rotate towards the fixed point but on the other they rotate away.
3. $-1<A/B<1$: the single fixed point has branched into two fixed points and in between fixed points objects rotate in opposite senses. Objects tend to rotate towards one fixed point (termed stable or an attractor) but rotate away from the other fixed point (termed unstable or a repeller).
4. $A/B=1$: the two fixed points of case 3 have reconverged into a single half-stable fixed point.
5. $A/B>1$: again there are no fixed points but all objects rotate with the same sense, but in the opposite sense to those in case 1.

In terms of non-linear dynamics the behaviour of the system can be summarised on a bifurcation diagram (see Fig. 4). This system exhibits a saddle-node bifurcation at $A/B=-1$ where a single fixed point is created and subsequently bifurcates into two fixed points as A/B increases. The behaviour of a rotating object depends on

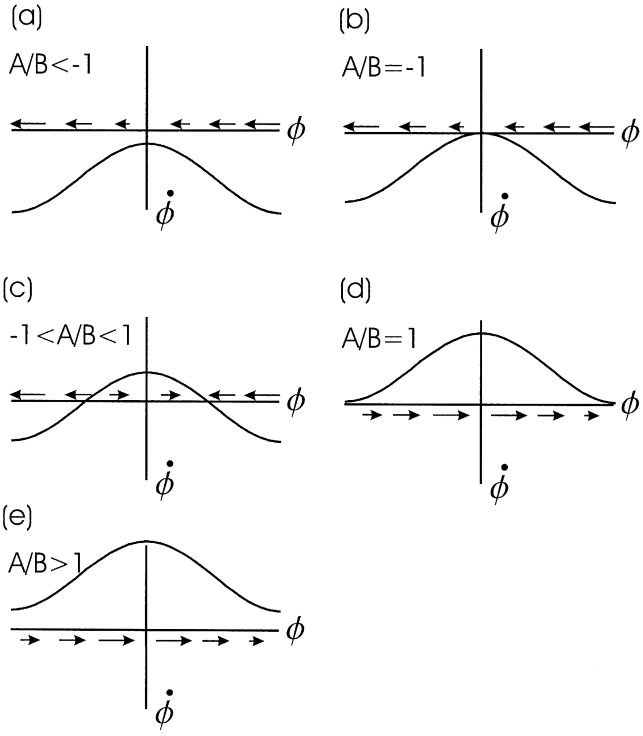

Fig. 3. Plots of $\dot{\phi}$ (rotation rate) against ϕ (object orientation). (a) $A/B<-1$, rotation rate is always negative (clockwise) although objects rotate more slowly for $\phi=0°$ and faster for $\phi=90°$. (b) $A/B=-1$, rotation rate is always negative (clockwise) except at $\phi=0°$ where the rotation rate is zero (a fixed point) implying that objects obtaining this orientation remain in that orientation. (c) $-1<A/B<1$, in this case there are both negative and positive rotations and two fixed points. The fixed point for $\phi<0°$ is unstable insofar as any perturbation away from it causes an object to continue to rotate away from it. The fixed point for $\phi>0°$ is stable and any perturbation away from it is immediately rectified by the object rotating back into the fixed point position. The cases shown in (d) and (e) are the reverse of (b) and (a), respectively (i.e. positive instead of negative rotation).

both A and B and therefore on both the flow field and the object axial ratio. For $A/B<-1$ objects rotate continuously whereas for $A/B=-1$ objects asymtotically rotate into parallelism with the half-stable fixed point orientation and for $-1<A/B<1$ objects asymtotically rotate into parallelism with the stable fixed point orientation. At $A/B=1$ the stable and unstable fixed points converge back into a single half-stable fixed point and for $A/B>1$ objects continuously rotate once again.

It is important to differentiate between continuously and asymptotically rotating objects. Because the axial ratio of tiled objects can be measured directly in the field, it is better to formulate the answer in terms of R. Objects continuously rotate for $|A/B|>1$, that is when:

$$W_k < -\frac{R^2-1}{R^2+1} \quad \text{or} \quad W_k > \frac{R^2-1}{R^2+1} \tag{13}$$

so that for $R=1$ all objects are spherical and continuously rotate at a constant rate independent of W_k, although for $W_k=0$ the rotation rate is zero, whereas for $R=2$, all

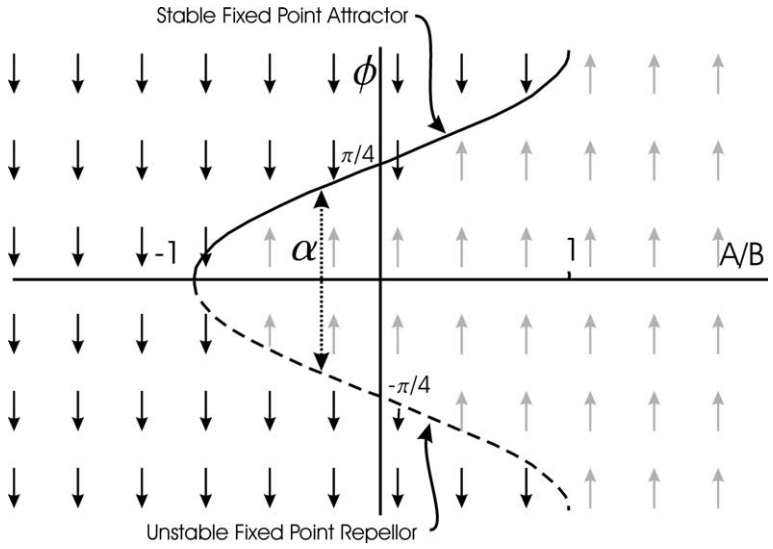

Fig. 4. Bifurcation diagram of rotation of elliptical objects where orientation (ϕ) is plotted against A/B and dark arrows represent negative rotation and light arrows positive rotation. For $A/B<-1$ all objects rotate negatively; however, when $A/B=-1$ a saddle node bifurcation occurs where a single fixed point develops and for $-1<A/B<1$ the single fixed point bifurcates into a pair of stable and unstable fixed points. At $A/B=1$ the pair of fixed points merge once more into a single fixed point and there are no stable positions for $A/B>1$.

objects continuously rotate only when $W_k<-0.6$ or $W_k>0.6$. From Fig. 5 it is evident that for asymptotically rotating objects to occur over a substantial range of W_k objects must have an axial ratio greater than approximately three.

The angles subtended between the fixed point orientations are related to W_k. The fixed point orientations are found by equating Eq. (11) to zero and then solving for ϕ:

$$\phi = \pm\frac{1}{2}\cos^{-1}\left(\frac{1+R^2}{1-R^2}W_k\right) \tag{14}$$

so that the angle between the fixed point orientations (α) is:

$$\alpha = \cos^{-1}\left(\frac{1+R^2}{1-R^2}W_k\right) \tag{15}$$

As R becomes large, then the behaviour of the object approaches that of a passive line and the angle between fixed point orientations approaches that of the flow apophyses discussed in the previous section (see Fig. 6) and is given by:

$$\alpha_\infty = \cos^{-1}(-W_k) \tag{16}$$

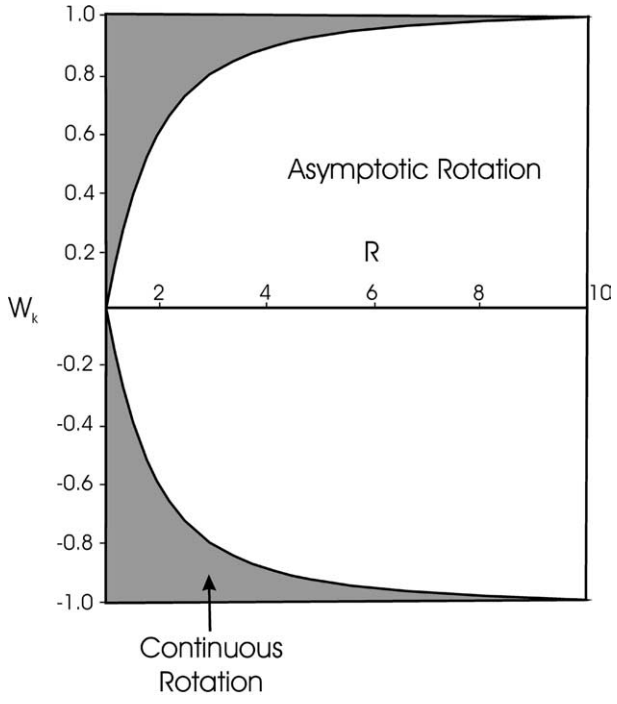

Fig. 5. W_k versus R with regions where continuous and asymptotic rotation occurs identified.

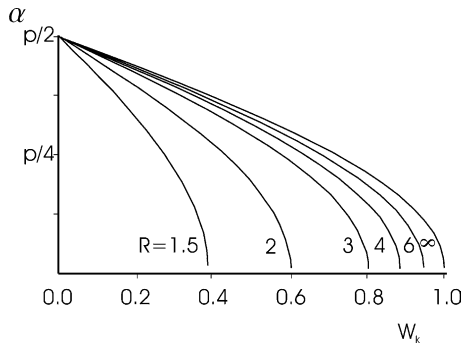

Fig. 6. Relationship between the angle between fixed points (α), aspect ratio (R) and W_k. The angle between the flow apophyses is given by $R=\infty$.

4. Confidence intervals for proportional statistics

As with most geological measurements, there are errors associated with individual observations as well as errors arising from the fact that the ultimate calculation is based on a sample of the total population. It is rarely if ever possible to observe the total population. Therefore it is good practice to quote a reasonable confidence interval for any calculated value. For example, giving a value with a 95% confidence interval means that there is a 0.95 probability that the true value lies within the quoted interval. The relationship between W_k and tiling presented below will be based on the proportion M of dextrally (or sinistrally) tiling pairs and statistics of rates and proportions are well studied (Fleiss, 1981).

Fleiss (1981, p. 14) gives expressions for the upper and lower limits of a single proportion and these are adapted to give expressions for upper and lower limits for M (i.e. M_L and M_U):

$$= \frac{(2nM + z^2 - 1) \pm z\sqrt{z^2 - (2 + 1/n) + 4M(n(1 - M) + 1)}}{2(n + z^2)} \tag{17}$$

where n is the total sample size and z is a percentile of the standard normal distribution (where a value of 1.96 gives the 95% confidence interval for M). The upper interval is generated by using the positive sign and vice versa for the lower interval. In most standard statistics texts (see, for example, Devore, 1995, p. 288) a much simpler version of the above confidence interval is given, which specifically assumes that the proportion M is of moderate value, i.e. $0.3 < M < 0.7$. The simpler version does not apply for very high or low values of M, which is clearly a possibility in the present situation. Inferences about M may be made using the binomial probability distribution but when $nM \geq 5$ and $n(M-1) \geq 5$ the binomial distribution is well approximated by the normal distribution (Devore, 1995, p. 163). This assumption is used in deriving Eq. (17) (Fleiss, 1981, p. 13). A plot of the confidence intervals is shown in Fig. 7a for $n = 100$. The upper and lower intervals are generally asymmetric and include lower bounds for $M = 100\%$ and upper bounds for $M = 0\%$. In the simplified case, there are no bounds for $M = 100$ or 0%, i.e. erroneously implying that the error is zero.

By taking the derivative of the difference between M_U and M_L, and equating with zero, it is found that the maximum error occurs for a value of M:

$$M = \frac{1}{2} - \frac{1}{2n} \tag{18}$$

Therefore substituting this value into Eq. (17), the relationship between maximum error and population size is obtained:

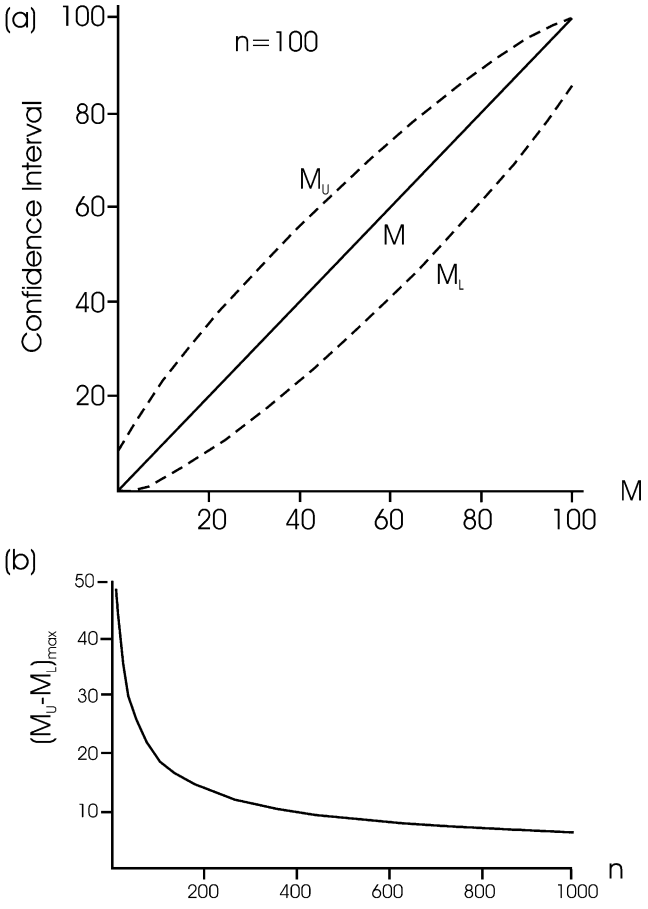

Fig. 7. (a) Relationship between observed proportion (M) in percent and upper and lower confidence interval (M_U and M_L) for 100 data. (b) Graph of variation of maximum confidence interval against the number of data. For n less than approximately 200, the confidence interval is large.

$$(M_U - M_L)_{max} = \frac{z}{\sqrt{n + z^2}} \tag{19}$$

In order to estimate an acceptable minimum sample size the maximum confidence interval size $(M_U - M_L)_{max}$ is plotted against sample size n (Fig. 7b) for $z = 1.96$ (i.e. 95% confidence interval). These graphs show firstly the dependence of confidence interval on the proportion and secondly that in order to obtain a maximum confidence interval of less than approximately 15% (i.e. $\pm 7.5\%$ on average), at least 200 readings should be used.

The confidence intervals described here are entirely due to sampling errors and should be treated as a minimum estimate as they do not take into account errors from other sources. Additional errors may arise due to (1) erroneous identification of tiling in the field, (2) the assumption of flow homogeneity being inaccurate and the flow-type may have in fact rapidly varied spatially, (3) the flow-type may have varied over time and may not have been steady-state and (4) Jeffery's (1922) model for rotation (see next section) assumes isolated objects whereas the model here assumes object interaction.

5. Mathematical model of tiling

5.1. Introduction

The relationship between magmatic tiling characteristics and flow kinematics is studied here by numerically simulating the development of tiling across a range of values for W_k Although the development of tiling is phenomenologically simple, i.e. two objects collide, it is conceptually difficult to decide whether two initially placed objects will end up tiling or not because each object is both rotating and relatively translating due to the bulk flow kinematics. The approach taken here is simplistic but insightful and any assumptions and corresponding limitations are fully acknowledged throughout.

5.2. Phenocryst motion

Firstly the rotation of each object is modelled using Eq (12), which has the following solution:

$$\phi(t) = -\tan^{-1}\left[\frac{\alpha\tanh(\alpha t + \tanh^{-1}\beta)}{A - B}\right] \tag{20}$$

where $\alpha = \sqrt{B^2 - A^2}$, $\beta = (\alpha\tan\phi_0)/(A + B)$ and ϕ_0 is the initial orientation of the ellipse long axis. However, extreme care is required when applying this equation because β can take on large values outside the range of $\tan^{-1}$ and the following special cases need to be observed:

if $B^2 - A^2 > 0$ and $\beta > 1$

$$\phi(t) = -\tan^{-1}\left[\frac{\alpha(e^{\gamma_1} + e^{-\gamma_1})}{(A - B)(e^{\gamma_1} - e^{-\gamma_1})}\right]$$

if $B^2 - A^2 > 0$ and $-1 < \beta < 1$

$$\phi(t) = -\tan^{-1}\left[\frac{\alpha\tanh(\alpha t + \tanh^{-1}\beta)}{A - B}\right]$$

if $B^2 - A^2 > 0$ and $\beta < -1$

$$\phi(t) = -\tan^{-1}\left[\frac{\alpha(e^{\gamma_2} + e^{-\gamma_2})}{(A - B)(e^{\gamma_2} - e^{-\gamma_2})}\right]$$

if $B^2 - A^2 < 0$ $\phi(t) = \tan^{-1}\left[\frac{\alpha\tan(\alpha t + \tan^{-1}\beta)}{A - B}\right]$

where:

$$\gamma_1 = \alpha t + \frac{1}{2}(\ln(\beta + 1) - \ln(\beta - 1))$$

$$\gamma_2 = \alpha t + \frac{1}{2}(\ln(-\beta - 1) - \ln(-\beta + 1))$$

Modelling the rotation of phenocrysts by the equations of Jeffery's (1922) serves only as a first approximation. This is because Jeffery's (1922) model assumes a single object in isolation; however, in the present model objects interact. Therefore around a single object the velocity field is disturbed (Jeffery, 1922; Jezek et al., 1999; Mandal et al., 2001; Samanta et al., 2003), which should affect the behaviour of nearby objects. This type of interaction is not taken into account in the present model. However, no analytical solution to this problem presently exists and although a numerical solution is possible it is practically and computationally unfeasible to perform the hundreds of thousands of runs in order to achieve the results obtained here using the first order approximation.

Secondly the relative motion of nearby objects is modelled by solving Eq. (3) given the particular form of **L** (Eq. (5)). This leads to the following system of ordinary differential equations:

$$\frac{dx_1}{dt} = L_{12}x_2$$

$$\frac{dx_2}{dt} = L_{21}x_1$$

which have the following solution for an object whose centroid is (x_{10}, x_{20}):

$$x_1(t) = x_{10}\cosh(\omega t) + x_{20}\xi\sinh(\omega t)$$

$$x_2(t) = \frac{x_{10}}{\xi}\sinh(\omega t) + x_{20}\cosh(\omega t)$$

where $\omega = \sqrt{L_{12}L_{21}}$ and $\xi = \sqrt{L_{12}/L_{21}}$. Caution is required if $L_{12}L_{21} < 0$ as account must be taken of the impact of complex numbers on the solution; however, the following identities, $\cosh(ix) = \cos(x)$ and $\sinh(ix) = i\sin(x)$, take care of any modifications required. In the case where either of L_{12} or L_{21} take the value zero, we have the following limiting cases: for $L_{12} = 0$:

$$x_1(t) = x_{10}$$

$$x_2(t) = x_{10}L_{21}t + x_{20}$$

and for $L_{21} = 0$:

$$x_1(t) = x_{10} + x_{20}L_{12}t$$

$$x_2(t) = x_{20}$$

which correspond to simple shear parallel to the x_2 and x_1 directions, respectively.

Combining the rotational and translational components of phenocryst motion results in complex overall motions. These motions are difficult to visualise and this difficulty is compounded when trying to conceive how two such objects may interact. Accordingly the model is studied in detail by computer (see Section 5.4); however, it is necessary to consider at least a subset of these motions in order to appreciate the results (see for example the particular results in Fig. 16).

Modelling the relative displacement of phenocrysts using the above-mentioned equations is reasonable, although, once again perturbations of the velocity field due to the presence of objects will distort particle paths. However, in the absence of an analytical solution this is the best approach at present. Note that in the present model only pairs of objects of the same shape, size and initial orientation (i.e. parallel) are considered.

5.3. Determining sense of tiling

Determining the sense of tiling is intuitive; however, in order to mathematically analyse the problem in hand, a stricter definition of tiling (in two dimensions) is required With reference to Fig. 8 the following procedure is proposed. First select one of the tiled pair (it does not matter which one) and denote its centre point by q and denote the centre of the other object by s. Identify the centre point of the short side of the object with centre q that is closest to s, and denote it by r. Construct the vectors $\mathbf{u}$ and $\mathbf{v}$ from q to r and q to s, respectively. The sense of tiling is given by the third component of the cross product:

$$\frac{\mathbf{u}\times\mathbf{v}}{|\mathbf{u}\times\mathbf{v}|}$$

where $+1$ indicates a dextral sense and -1 a sinistral sense.

The definition just given includes end-on-end tiling as well as side-by-side tiling (see Fig. 9). However, it is important to distinguish between end-on-end and side-by-side tiling as most practitioners consider (and probably observe) only the side-by-side variety. The vectors $\mathbf{u}$ and $\mathbf{v}$ are used again and from the definition of the cross product in 2D:

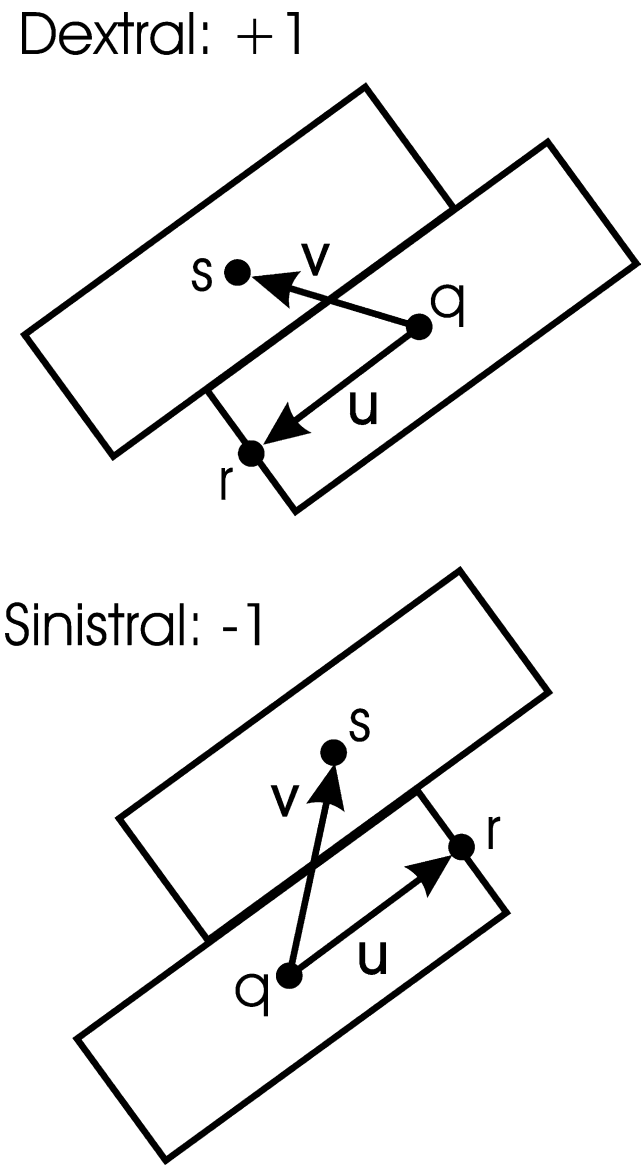

Fig. 8. Reference diagram for determining sense of shear from a tiled pair of objects.

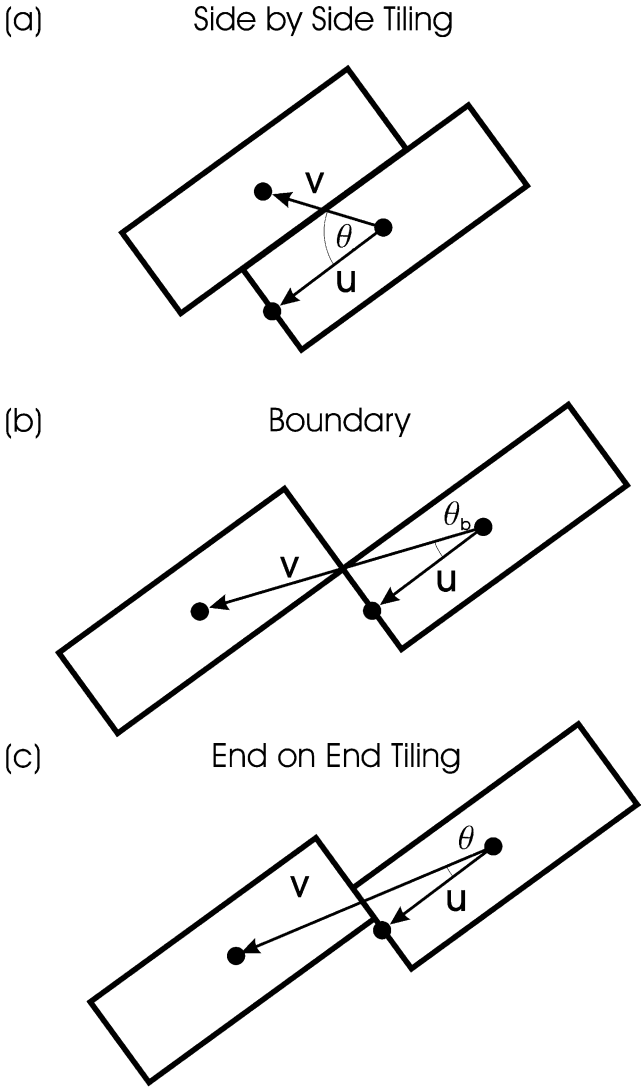

Fig. 9. (a) Side-by-side tiling occurs for $\sin\theta \geq \sin\theta_b$. (b) The angle θ_b is defined when the crystals make contact at a single point. (c) End-on-end tiling occurs when $\sin\theta < \sin\theta_b$.

$$\sin\theta = \frac{|\mathbf{u}\times\mathbf{v}|}{|\mathbf{u}||\mathbf{v}|}$$

where θ is the angle between **u** and **v**. The boundary between side-by-side and end-on-end tiling occurs where the crystals touch at corners so that **v** parallels the crystal diagonal (see Fig. 9). If the boundary angle is denoted by θ_b, then for end-on-end tiling $\sin\theta < \sin\theta_b$ and for side-by-side tiling we have $\sin\theta \geq \sin\theta_b$.

5.4. Software and analysis

In order to investigate the relationship between magmatic tiling, flow kinematics and crystal spacing software was written in C++ to simulate the evolution of a pair of objects behaving according to the equations given above The geometry is arranged as shown in Fig. 10 where each object has a long axis of length $2a$ and a short axis of length $2b=1$ so that the axial ratio $R=2a$. Object centroids are separated by a distance d, which can be viewed as a percentage (p) of the long axis length $2a$. The objects are both initially oriented with angle ϕ_{obj} (i.e. are parallel to each other) and the line joining their centroids has an initial orientation of ϕ_l. Both angles are randomly selected from a uniform distribution on the $[0, \pi]$ interval.

The analysis proceeded by first selecting a value for R (we studied $R=2.0$, 2.5, 3.0, 3.5, 4.0) and then taking $p=$ 50, 75, 100, 125, 150, 200 and 250%. For each p, the flow for $L_{12}=1$ and $L_{21}=-0.2$ up to 1.0 in 0.02 steps was investigated (i.e. corresponding to $W_k=1.5$ to 0). For each combination of axial ratio, separation and flow, the initial relative positions and orientations of two objects were continuously generated by obtaining values for ϕ_{obj} and ϕ_l from the uniform distribution, and then allowed to evolve, until such time as there were a total of 1000 dextrally or sinistrally tiled object pairs were measured or a total of 35,000 attempts were made. For each value of ϕ_{obj} and ϕ_l there can be six possible outcomes: (1) dextrally tiled, side-by-side pair, (2) dextrally tiled, end-on-end pair, (3) sinistrally tiled, side-by-side pair, (4) sinistrally tiled, end-on-end pair, (5) non-tiled pair, (6) bad initial position (e.g. they were overlapping to begin with—a physically impossible condition).

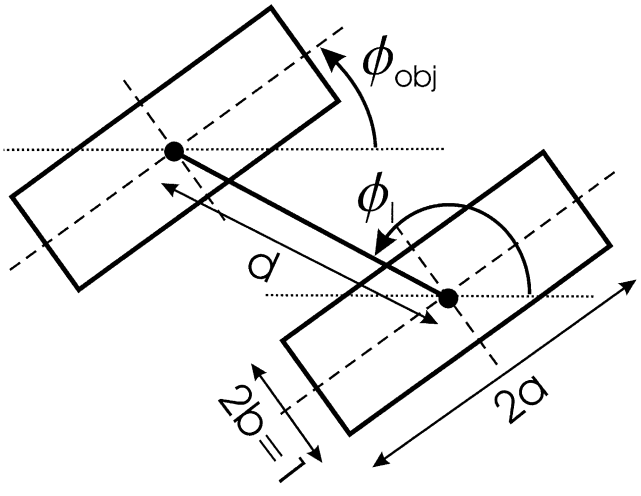

Fig. 10. Definition diagram for ϕ_{obj}, ϕ_l and d.

Detecting the non-tiled outcome may pose some difficulty. For $W_k<1.0$ crystals tend to move apart so that once a threshold distance has been surpassed then it is certain that the crystals will not interact, whereas for $W_k>1.0$ the pulsating nature of the flow implies that crystal pairs periodically move closer together then further apart. Additionally, the period of rotation of the crystals is always less than that of the flow, making interaction detection even more difficult. In this implementation, the no tiling outcome was detected by a lack of interaction after a suitably long period of time. End-on-end tiling has not been observed in the field but is a real feature of the model as a possible outcome. However, in the next section it is seen that end-on-end tiling only occurs for $W_k>1$, possibly explaining the absence of this phenomena in the field. Alternatively, it may be that this structure is not as stable as side-by-side tiling and thus does not survive.

Crystal spacing greater than 250% is not considered in the analysis because 250% corresponds to a crystal fraction of less than 10%, i.e. a low density or concentration of crystals. At even lower crystal concentrations particle interactions becomes less probable and therefore tiling is less likely to be observed. However, even at low concentrations, tiling would eventually occur if the simulation were left to run long enough.

In this study the relationship of tiling to finite strain is not investigated. Tikoff and Teyssier (1994) presented the results of a simulation study of porphyroclast interaction and demonstrated a sharp increase in density of clast imbrication with increasing finite strain (for W_k between 0 and 1). Therefore it is expected that tiling density would also increase with finite strain. However, in the case of pulsating strain histories the situation could occur whereby tiling density increases while finite strain values fall. More accurately then, tilting density should increase with the duration of the flow. In the current study the relationship with flow-type is being studied so that by letting object pairs evolve to one of the six outcomes above, is in effect ignoring the influence of finite strain or duration of flow.

5.5. Relationship between initial spacing and crystal fraction

In the methodology outlined above one of the key variables is the initial separation (i e. d or p); however, igneous petrologists normally talk in terms of crystal or melt fractions rather than spacings. Furthermore the observed crystal fraction (f_c) is relatively easy to measure in practice, whereas estimating the initial spacing poses more problems for measurement. Therefore a relationship between initial spacing and crystal fraction is required. Crystal fraction is

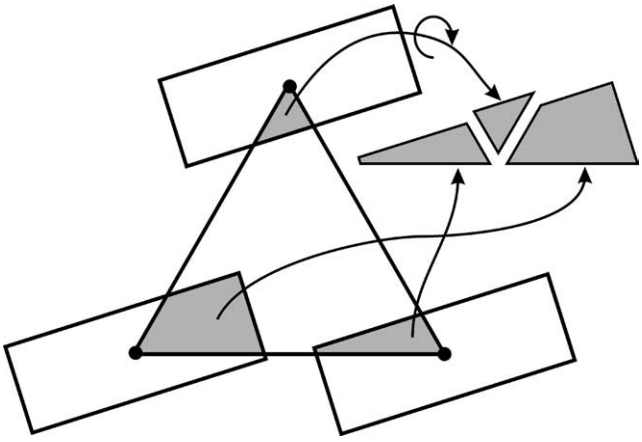

Fig. 11. Consider an equilateral triangle of edge length $d=2ap/100$, with three objects of identical size and orientation placed at each vertex. This is a graphical illustration that the area of overlap between the triangle and the objects is equal to half the area of one such object.

simply the percentage volume or area occupied by a crystal species of interest, in the current case, tiling phenocrysts. The model studied here is 2D and thus crystal fraction is a percentage area.

In the model studied above, pairs of objects are always generated with a spacing of d; therefore, it is reasonable to assume that the average spacing of the crystal population is also d. From this we can construct the average situation whereby three crystals are d apart from each other, necessitating in an equilateral triangle as shown in Fig. 11. The crystal fraction is the ratio of the combined areas of the crystals overlapping with the triangle, to the total area of the triangle. In the model studied all three crystals are of the same size and in the simple case of all three having the same orientation, graphical arguments (see Fig. 11) indicate that the overlap area sums to half the area of one crystal. Integral mathematics indicates that for three arbitrarily, but not identically, shaped objects of the same area whose orientations are randomly selected from the uniform distribution on $[0, \pi]$, arranged in any triangle (i.e. not necessarily an equilateral triangle) also overlap by half the area of one such object (see Appendix A).

In the present case the area of the triangle is given by:

$$\frac{1}{2}d^2\sin 60^\circ = \frac{\sqrt{3}}{4}d^2 = \frac{\sqrt{3}}{10000}p^2a^2$$

The area of one object in the present case is $2a=R$, so the crystal fraction (as a percentage) is therefore:

$$f_c = \frac{2000000}{\sqrt{3}p^2R}$$

Fig. 12 illustrates the crystal fraction for parameter values considered in the present study and indicates that for initial spacings ≥ 100, the crystal fraction is below the RCMP threshold above which predominantly solid-state deformation processes are thought to occur. At $p \approx 150$ the crystal fraction is below 20%, whereas for $p \geq 200$ the crystal fraction is below 10%. In other words, the model parameters considered here reflect a range of crystal fractions from very high to very low.

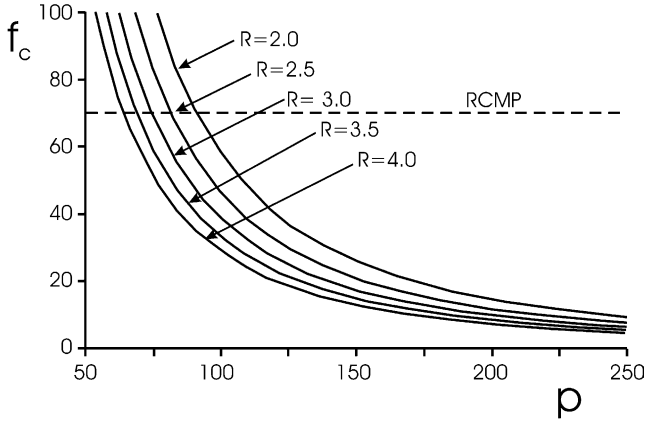

Fig. 12. Relationship between crystal fraction (f_c) and spacing (p) for different aspect ratios.

6. Results

The numerical experiments generated a large quantity of data, which is summarised graphically in Figs. 13–15. There are a number of remarkable features illustrated by this data, noting that the shear sense of the flow is dextral for $W_k > 0$. Only minor variations in observed patterns occurred for different tile aspect ratios (R), therefore the results for $R=3.0$ are representative and are examined in detail. First of all the relative importance of the various outcomes are presented in Fig. 13 as percentages. For example, Fig. 13a displays the percentage of side-by-side tiled pairs compared with the total number of crystal pairs. Side-by-side tiling is common for low spacings but becomes rare for high spacings, largely independent of W_k. That being said there is a slight change in behaviour for $W_k > 1$. By contrast, end-on-end tiling is generally of minor importance but is significant for $W_k > 1$ (see Fig. 13b). However, as mentioned earlier, the absence of field-based observations of end-on-end tiling may indicate that super-shear is not common in nature. The occurrence of no tiling becomes dominant for high spacing emphasising that tiling occurrence is strongly related to initial spacing (see Fig. 13c). This study therefore indicates that it may be possible to relate the frequency of occurrence of tiled pairs in the field to the density of crystals present at the time of fluid flow. Fig. 13c also highlights a change of behaviour of the system for $W_k > 1$, whereby the occurrence

Fig. 13. Plots of percent occurrence of (a) side-by-side tiling pairs (b) end-on-end tiling pairs and (c) no tiling pairs compared with total pairs against W_k for an object aspect ratio of $R=3$ and a variety of initial spacings.

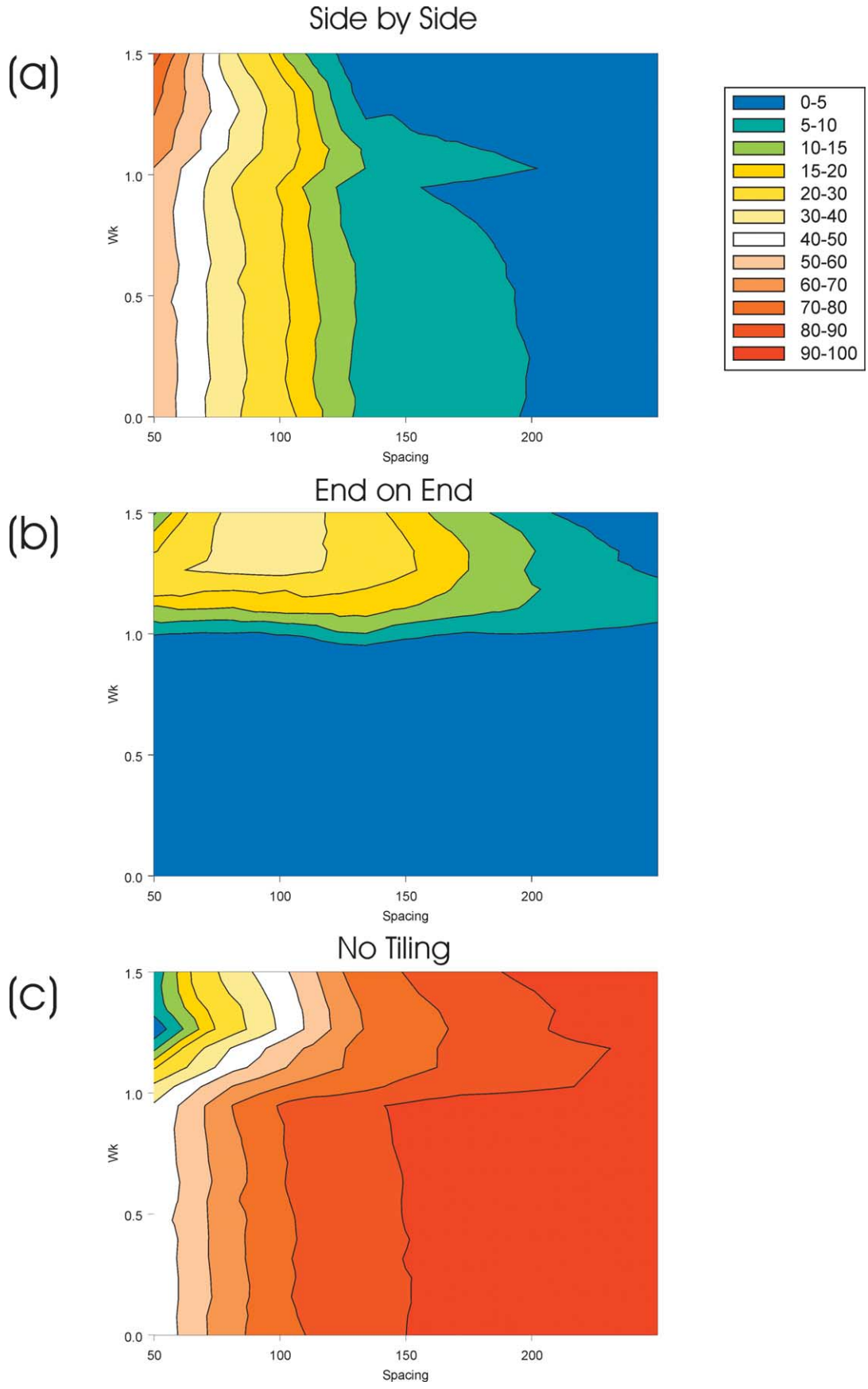
Side by Side
(a)
1.5
1.0
0.5
0.0
Wk
50
100
150
200
Spacing
0-5
5-10
10-15
15-20
20-30
30-40
40-50
50-60
60-70
70-80
80-90
90-100
End on End
(b)
1.5
1.0
0.5
0.0
Wk
50
100
150
200
Spacing
No Tiling
(c)
1.5
1.0
0.5
0.0
Wk
50
100
150
200
Spacing

of no tiling is less common for $W_k > 1$, presumably due to the occurrence of end-on-end tiling.

Fig. 14 presents the relationship between the proportion of dextral tiling, spacing and W_k. Again there is a clear behavioural distinction between $W_k < 1$ and $W_k > 1$. Fig. 14a illustrates the relationship for side-by-side tiling. At $W_k = 0$ there is a 50/50 occurrence of dextral/sinistral tiling followed by an upward trend to predominantly dextral tiling at $W_k = 1.0$. For low spacing ($p < 75\%$) the upward trend is minor but becomes more pronounced for higher spacings. For $W_k > 1$ (super shear) the dominance of side-by-side dextral tiling diminishes and at high spacing sinistral side-by-side tiling predominates. There is a clear and dramatic change of behaviour under super shear flow. End-on-end tiling presents a variable pattern (Fig. 14b) for $W_k < 1$ reflecting its rarity in this regime. It is important to be cognisant of the frequency relationships in Fig. 13 when interpreting the data in Fig. 14. The total tiling proportion patterns in Fig. 14c reflect the dominance of side-by-side tiling ($W_k < 1$) and end-on-end tiling ($W_k > 1$) in different behavioural regions.

This study highlights that not only is there a relationship between tiling proportion and flow type, but the exact nature of the relationship depends strongly on the average initial spacing of the rotating objects. It also demonstrates that even under dextral simple shear (where all objects rotate dextrally) there can be a significant proportion of sinistrally tiling pairs. In most cases, there are a minimum of 20–30% of object pairs tiling with the opposite sense to that of the flow shear sense. This clearly illustrates the danger in assigning a simple shear flow type and shear sense on the basis of a few observations of crystal tiling.

In Fig. 15 detailed results for the numerical model for $R = 3.0$ and initial spacings of 50, 75, 100, 125 and 150% (i.e. $f_c = 154.0$, 68.5, 38.5, 24.6 and 17.1%, respectively) are presented for $W_k = 0.0$, 1.0 and 1.5. Black portions (i.e. no points) are regions where impossible start conditions occur and are found for ϕ_{obj} close to ϕ_1. The extent of this region is primarily related to initial spacing and also to object aspect ratio. Low p-values result in a large amount of impossible start positions whereas for p greater than approximately 100 there are no impossible start positions as the two objects are too far apart to initially interact. The rest of the diagram is filled with the result of starting from a particular position. In general there is a regular pattern and arrangement of the different regions giving dextral, sinistral and no tiling. In general for $W_k < 1$, the various regions remain quite distinct, independent of parameter values and no mixed regions occur which might indicate extremely complex/chaotic behaviour. However for $W_k = 1.5$, some mixing is evident for $p > 100$ (Fig. 15), which may indicate more complex behaviour in this region.

There are a number of general trends evident in the detailed data consistent with the summary data of Figs. 13 and 14. The proportion of no tiling (i.e. red) increases as the crystal fraction decreases, hence the density of tiling behaviour in Fig. 13. As W_k goes from 0.0 (pure shear) to 1.0 (simple shear) the blue area of side-by-side dextral tiling increases from 50/50 to predominate, reflecting the relationships illustrated in Fig. 14. For low crystal fractions the region where tiling can occur becomes a very thin strip, although in every case there still remains a sizeable portion where tiling opposite to the fluid shear sense can occur. End-on-end tiling predominates for $W_k > 1$ but also occurs for high p and $W_k < 1$, but is subordinate to side-by-side tiling.

In Fig. 16a and b the evolution of an object pair is illustrated for $W_k = 0$, $R = 3.0$ and $p = 125\%$. It is clear that different starting positions lead to different senses of tiling. In Fig. 16b and c all parameters are the same as for Fig. 16a and b except that the flow type is simple shear (i.e. $W_k = 0$). Again, different starting positions can lead to both dextral and sinistral tiling even though the sense of simple shear is dextral.

7. Application to and re-analysis of a natural example

Blumenfeld and Bouchez (1988) reported the tiling characteristics of the Barbey–Seroux granite located in north eastern France in the Vosges massif and this remains the most comprehensive published study of tiling and tiling data. They measured the sense of shear indicated by tiled K-feldspar megacryst pairs in both the *XZ* plane (i.e. normal to foliation and parallel to lineation) and *XY* plane (i.e. normal to foliation and lineation). In the *XY* section, Blumenfeld and Bouchez (1988) demonstrate the occurrence of sinistral and dextral tiling in close to equal proportions, which they interpret as indicative of 2D pure shear (i.e. $W_k = 0.0$, which agrees with the results presented above). Because they present only summary data for the *XY* section a more detailed analysis, including confidence intervals, cannot be executed. However, they do present detailed data for the *XZ* section.

A simplified cross-section including dextral tiling proportions (M) and numbers of observations (n) from the *XZ* section sample data of Blumenfeld and Bouchez (1988) is schematically illustrated in Fig. 17a. In Fig. 17b an example of estimating W_k confidence intervals from calculated tiling proportion intervals is shown. In relating the data of Blumenfeld and Bouchez (1988) to the results of the current study, assumptions must be made about the initial spacing and aspect ratio of the phenocrysts. Regarding initial spacing it is noted that for f_c to be below the RCMP threshold it must be that $p > 100\%$ (see Fig. 12). Furthermore from Fig. 14 with $p > 100\%$ it is noted that the exact value of the initial spacing does not greatly influence the form of the relationship between tiling proportion and W_k, so that choosing $p = 150\%$ (i.e. $f_c = 17.1\%$) will not affect the results of this analysis greatly. From photographs of the granite, it is reasonable to assume that on average $R = 3.0$. W_k values along with confidence

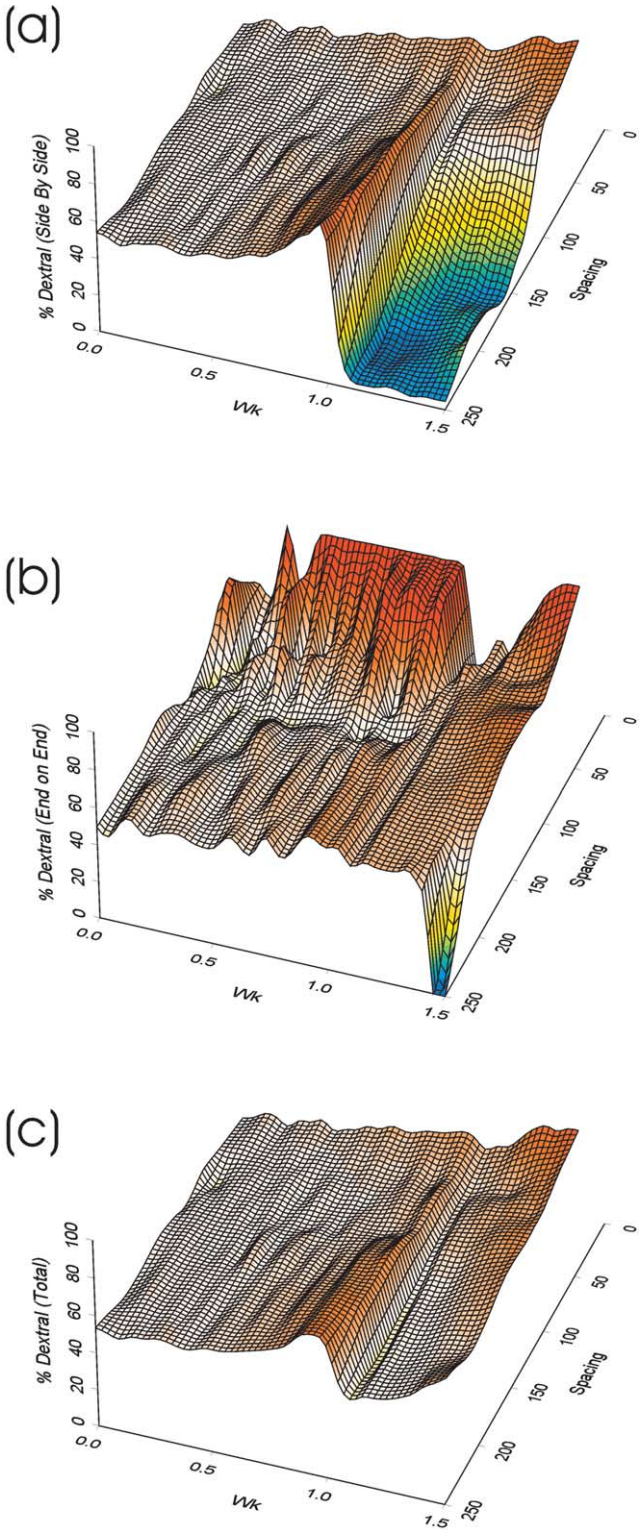

Fig. 14. Plots of proportion of (a) side-by-side dextral tiling pairs (b) end-on-end dextral tiling pairs and (c) total dextrally tiling pairs against W_k for an object aspect ratio of $R=3$ and a variety of initial spacings.

intervals calculated using the model developed here are given in Table 1.

This re-analysis study highlights the importance of sample size when utilising tiling to estimate the nature of deformation and shear sense. Only sample 2 ($n=363$) provides narrow enough bounds for W_k to confidently assert that a dextral simple shear deformation led to the observed tiling pattern. For all other samples $n\leq 110$, and in each case the exact type of deformation cannot be determined and could range from mixed pure/simple shear to simple shear (samples 1, 4, 5 and 6) or from pure shear to simple shear in the case of sample 3. In every case the correct (i.e. dextral—on the basis of sample 2) shear sense is determined even though the number of data is too low to restrict the exact flow type with any confidence. This suggests that for small samples sizes ($n\geq 60$) the shear sense may be determined. However, if the observed proportion is near to 50% then the confidence limits are likely to enclose a large range of W_k values so that much more than 60 observations may be required to restrict the flow-type and determine the shear sense.

The threshold of $n=60$ can also be derived from Eq. (19) for the maximum error, by finding the number of data which gives a maximum error (i.e. $(M_U-M_L)_{max}$) of 25%. Since the tiling proportion varies between 50 and 75% in Fig. 17, i.e. a range of 25%, then for precision the maximum error must be $\leq 25\%$ corresponding to $n\geq 60$. However, in order to determine the exact flow type much more data than 60 is required.

8. Discussion

In this paper we present the results of a simple mathematical model for tiling development in 2D, which takes into account object rotation and translation. We believe that this model provides new insights into the tiling phenomena. However, there are many assumptions incorporated into the model that should always be acknowledged. Primarily, the influence of the perturbed velocity field around rotating objects is ignored, only the evolution of initially parallel pairs of objects is considered and the model is restricted to 2D.

Assessing the relative importance of the perturbed velocity field is not possible at present because a general theory for the motion of adjacent particles does not exist. Ildefonse et al. (1992a) conducted experiments investigating adjacent particle interactions during simple shear and they found that adjacent particles tend to rotate slower than isolated particles (i.e. rotating according to the Jeffery's (1922) model). Except for the case of particles oriented initially parallel to the sense of shear, most adjacent particles remained within 5° of the theoretical prediction (see figs. 9–12 of Ildefonse et al., 1992a) for shear strains up to 1.2. More recently, Samanta et al. (2003) found similar effects both theoretically and experimentally for adjacent circular objects. In a detailed experiment illustrated in fig. 6 of Arbaret et al. (1996) $R=2.5$, $W_k=1$, $\phi_{obj}=90°$, $\phi_1=180°$ and $p\approx 75\%$ and by comparison with Fig. 15 the predictions of the present study agree with the observed sense of dextral

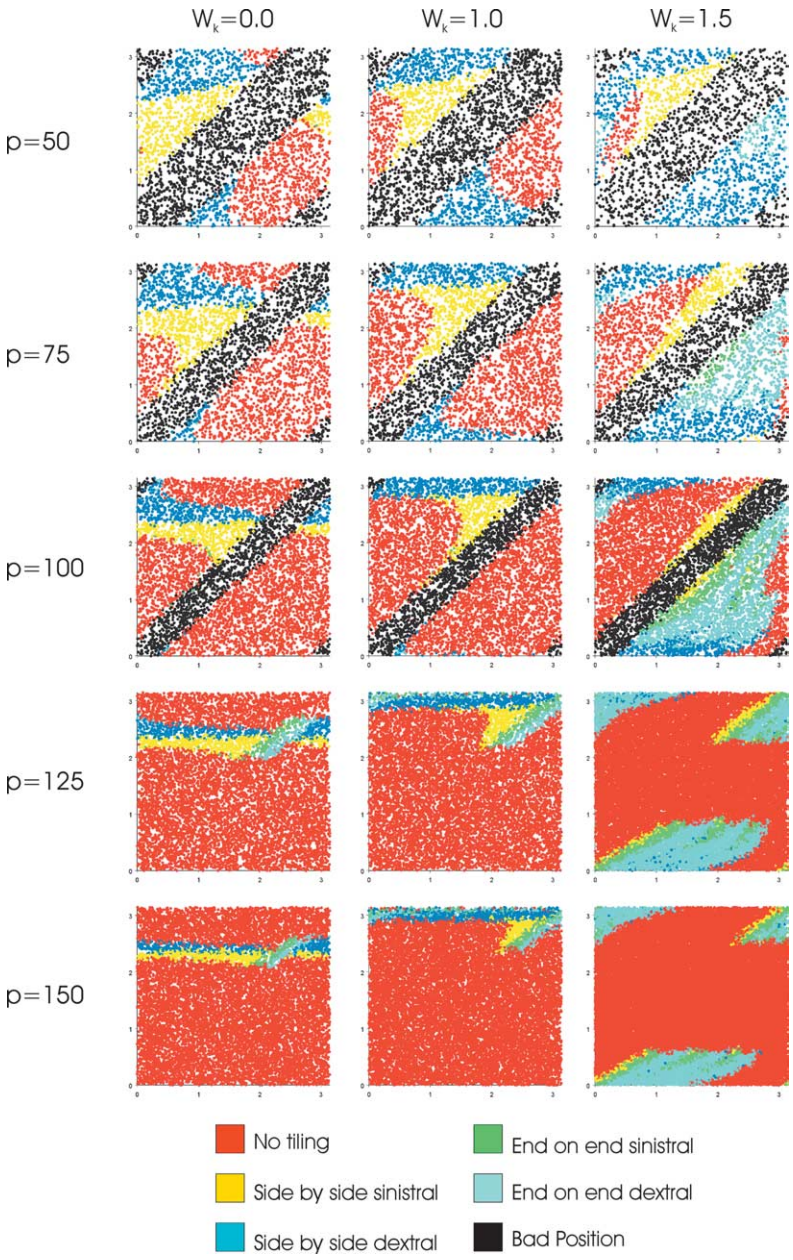

Fig. 15. Example of detailed results for $R=3$, showing multiple plots of outcome (i.e. tiling type) by initial position (ϕ_1 versus ϕ_{obj}) For low p there are black areas which represent invalid starting positions due to a physically impossible initial overlap.

tiling. These experimental results lend support to the validity of the current model and the assumption that although the perturbed velocity field around particles produces a noticeable effect, it is not sufficient to change the overall dynamics of the population. More advanced theories and models are required to fully address these issues.

Table 1
Results of the re-analysis of the data of Blumenfeld and Bouchez (1988)

Sample	n	Dextral (M)	Sinistral	M_L	M_U	W_{kL}	W_k	W_{kU}
1	60	73	27	59.7	81.9	0.84	1.04	1.06
2	363	67	33	61.8	71.5	0.90	0.97	1.02
3	110	59	41	49.2	67.3	≈0.1	0.82	0.98
4	63	68	32	54.9	77.5	0.63	0.99	1.07
5	52	75	25	60.7	84.0	0.88	1.04	1.06
6	72	68	32	55.8	77.0	0.78	0.99	1.07

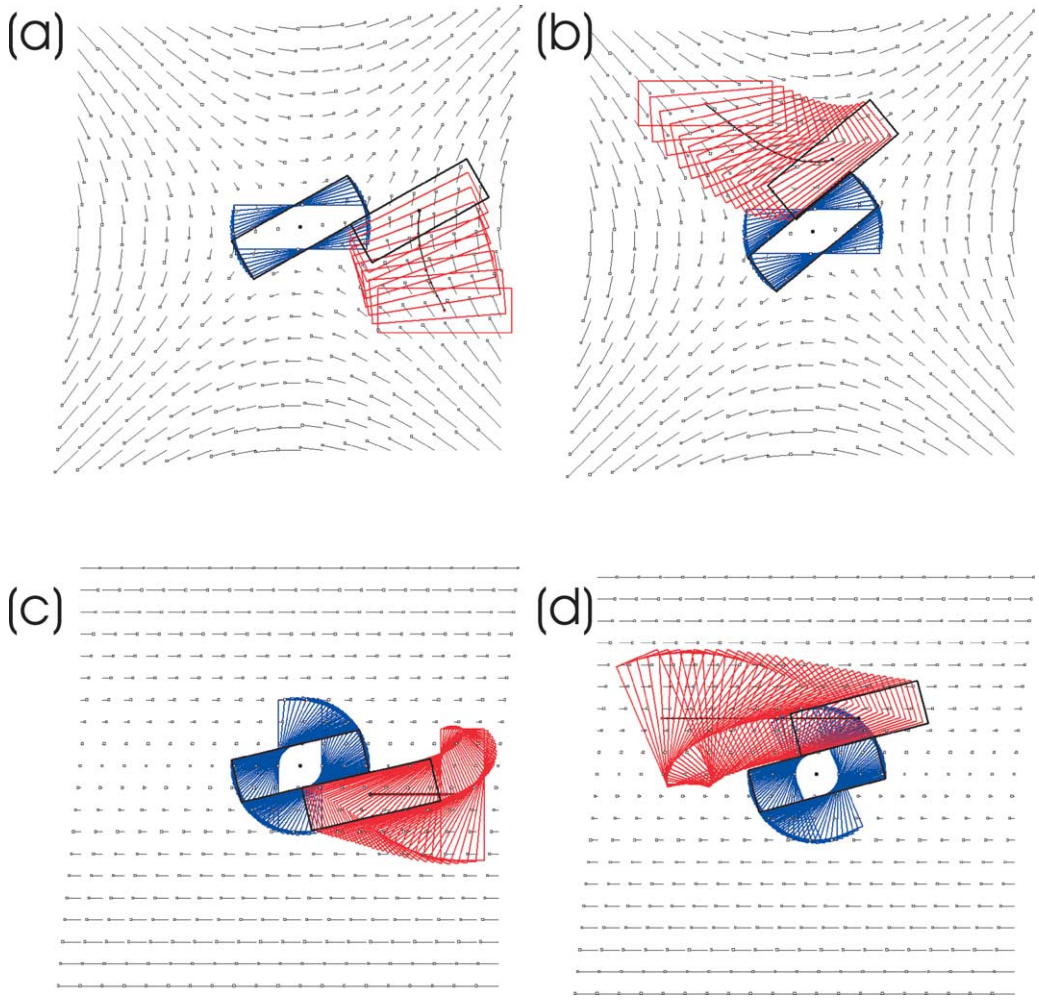

Fig. 16. Examples of tiling generated by the model for pure shear ((a) and (b)) and dextral simple shear flow ((c) and (d)). Arrows represent the local velocity field. Previous positions of the objects are drawn in red and blue and a continuous black line gives the path of the non-fixed objects centre point. Note that for dextral simple shear both dextral (concurring with the fluid flow shear sense) and sinistral (tiling sense opposite to that of the flow) tiling occurs.

The model is restricted to initially parallel pairs because assessing the sense of tiling of two touching non-parallel particle pairs is fraught with difficulties. More sophisticated models of particle behaviour need to be applied in order to provide a proper treatment of non-parallel particle pairs. The current model is restricted to 2D, whereas in practice crystals are 3D objects immersed in a fluid moving in 3D. The results presented here should only be considered with these assumptions in mind. It is hoped that future work will remove many of these assumptions and that more sophisticated and refined models can be investigated.

Blumenfeld and Bouchez (1988) reported approximately 70% dextrally tiled object pairs (shear sense to the SW) and therefore up to 30% of tiled pairs indicate the reverse shear sense. However, theoretical models (Ghosh and Ramberg, 1976; Fernandez et al., 1983) of simple shear indicate that all objects should rotate with the same shear sense (i.e. dextral in a dextral shear zone). Therefore, by considering rotation alone, there is an expectation that all tiled pairs should display the same shear sense. Blumenfeld and Bouchez (1988) suggested that the discrepancy between observation and theory might be explained by (i) the flow type departing from simple shear (W_k greater or less than one) or (ii) tiling interactions being due to both rotation and relative translation. The model presented here successfully reproduces the results of Blumenfeld and Bouchez (1988) by considering both rotation and relative translation and it is only by considering the more complex situation that realistic results can be achieved. The phenomena of tiled pairs with opposing shear senses does not require a departure from simple shear flow and according to this study it should be the rule rather than the exception. Therefore, the results presented here strongly support the second option of Blumenfeld and Bouchez (1988).

Analogue experiments by Arbaret et al. (1996) demonstrated that particle interaction is a process which takes place in low concentration suspensions, therefore tiling should not be restricted to high crystal fraction magmas as previously supposed (Ildefonse et al., 1992b; Nicholas, 1992; Tikoff and Teyssier, 1994). The present study further

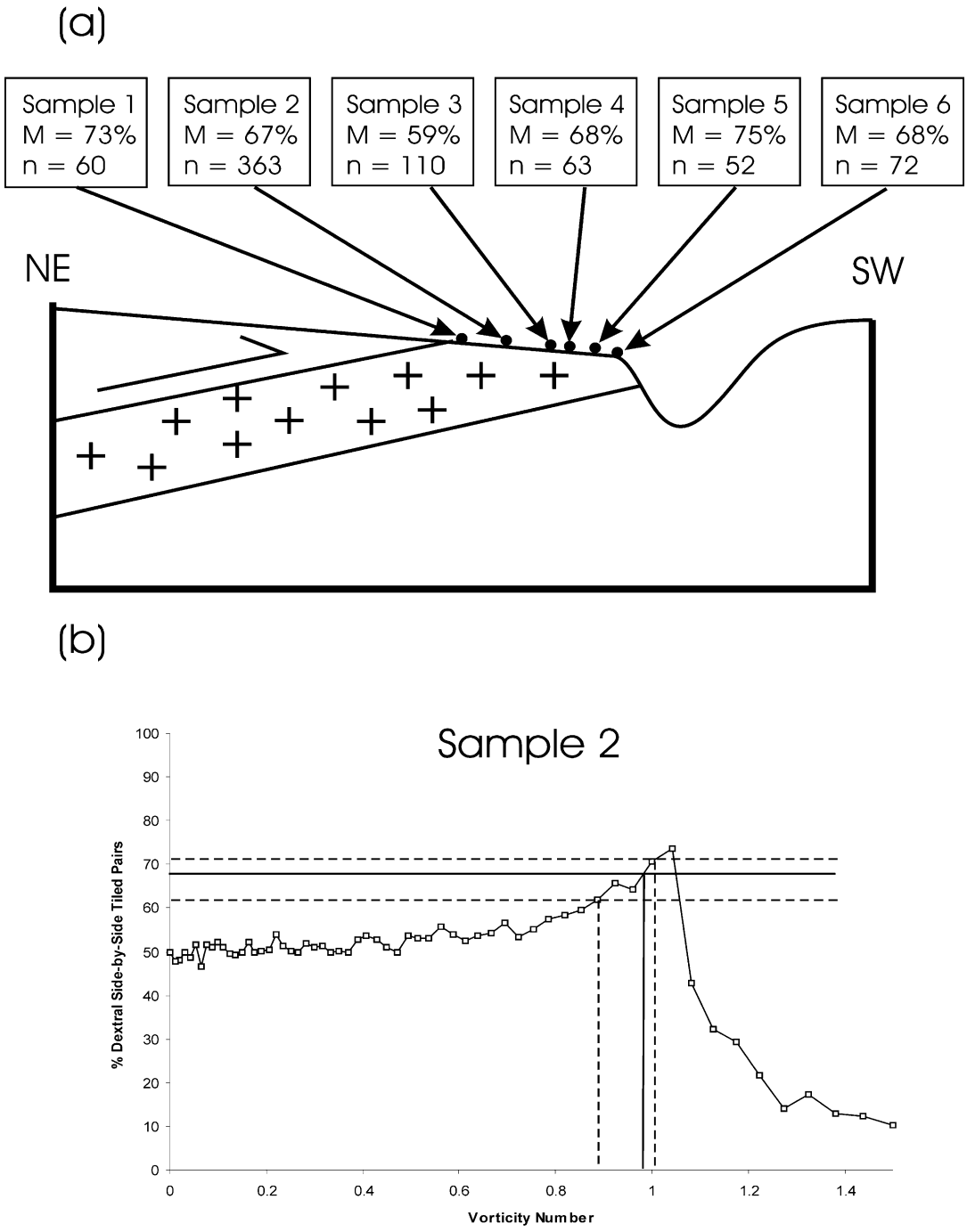

Fig. 17. (a) Schematic illustration of the Barbey–Seroux granite (after Blumenfeld and Bouchez, 1988) and sample locations. Note that here the section is viewed from the NW, whereas the original illustration was viewed from the SE; this change was made to integrate the example with the main body of the text, which mainly considers a dextral shear sense. (b) Example of how tiling proportion is related to W_k and estimation of confidence intervals for sample 2.

supports this view, which demonstrates a consistent variation in tiling proportion with W_k, object aspect ratio and also crystal fractions from high to low. Arbaret et al. (1996) also observed oppositely tiled pairs in their experiments. However, this occurred during the late stages of the evolution of the tiled pair (i.e. the separation phase). In the present study tiled pairs were not allowed to evolve beyond aggregation. More complex models need to be developed to assess the influence of extended object pair evolution on tiling proportions.

Tiling proportions have been shown to vary from 50% for $W_k=0$ up to approximately 70% for $W_k=1$ (the details depending on crystal fraction and object aspect ratios) for models based on crystal rotation and translation. However, it is very important to take into account the statistics of proportions when interpreting natural data and in general a

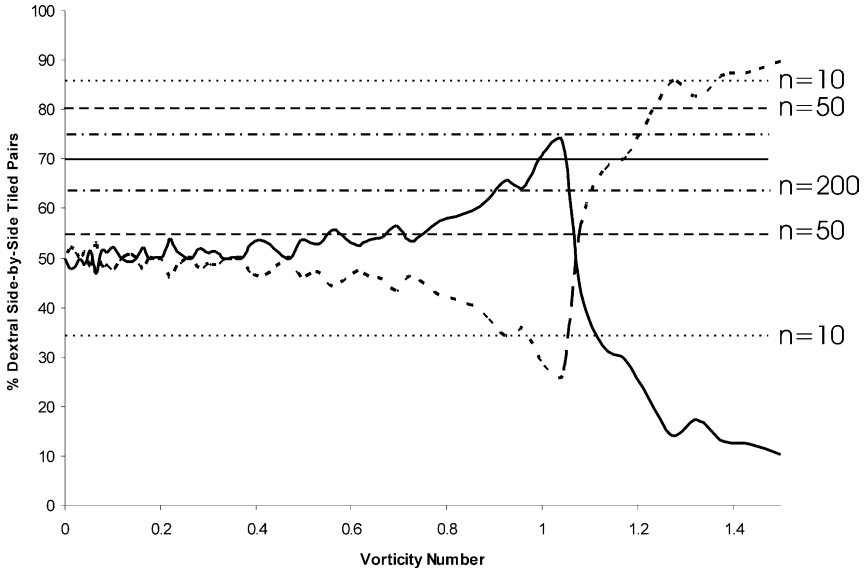

Fig. 18. Illustration of the relationship between sample size ($n=10$, 50, 200) and confidence intervals and how the interpretation of a tiling proportion may be affected. Here the dark horizontal line represents the observed 70% tiling proportion and the dotted/dashed horizontal lines represent the confidence intervals. The heavy (dextral) and dashed (sinistral) curves represent the tiling proportions predicted by the model.

large number of observations of tiling are required to determine W_k with confidence ($n \geq 200$). For example, consider the case of $p=150$ and $R=3.0$ shown in Fig. 18. Suppose that the observed proportion of dextrally tiling pairs is 70% (indicated by a horizontal solid line), which if taken to be absolutely correct indicates that $W_k \approx 1.0$. However, superposing 95% confidence intervals related to the number of observations changes the interpretation. If the tiling proportion is based on $n=10$ then W_k could be any value between 0 and 1.2 and the shear sense could be either sinistral or dextral. For $n \approx 50$ certainty regarding a dextral shear sense emerges, although W_k is in [0.7, 1.1] approximately. For $n=200$ W_k is in [0.9, 1.02] and now there is certainty regarding shear sense and flow type. Furthermore, due to the slow variation of tiling proportion with W_k near 50/50 tiling proportions, a large number of data are required to conclusively demonstrate a pure shear flow type.

At the beginning of this paper the uncertainty of Passchier and Trouw (1996 p. 127) of using tiling as a shear sense indicator was noted. The results of the model presented here allow some clarification of this point. Firstly the interpretation of shear sense based on a single tiled pair is undoubtedly erroneous. Furthermore, depending on the values of the parameters studied, there is a requirement for approximately 50–60 observations (over a region assumed to have undergone a steady state homogeneous deformation history) in order to determine shear sense and around 200 in order to give a reasonable estimate of W_k. Therefore a single tiled pair of crystals cannot be described as a shear sense indicator and the caution of Passchier and Trouw (1996) is justified.

The results presented here serve to motivate further research into this phenomenon. Experimental verification of the behaviours described here is required and more complex models that include long-term evolution (initiation, aggregation and separation as described by Arbaret et al. (1996)) and models that track the simultaneous evolution of large populations of objects need to be explored.

9. Conclusions

1. A mathematical model for the development of tiling including both rotation and relative translation was presented.
2. A consistent relationship between tiling proportions and W_k was found.
3. For pure shear there should be approximately 50% dextrally and 50% sinistrally tiled pairs, whereas for simple shear there should be around 70% of tiled pairs consistent with the shear sense.
4. This relationship is observed for high and low crystal fractions and a variety of object aspect ratios.
5. The density of tiling varies with the crystal fraction and it may be possible to use the frequency of occurrence of tiling to estimate the crystal fraction at the time of tiling.
6. By considering the statistics of proportions, it is shown that for shear sense determination at least 60 observations are required, whereas for estimation of W_k at least 200 observations should be taken.
7. A single observation of crystal tiling is a highly unreliable shear sense indicator.

Acknowledgements

We would like to thank Prof. Joao Hippert for handling the manuscript and Dr Joseph Jezek and an anonymous

reviewer for constructively criticising and improving the final version of this manuscript.

Appendix A

Appendix A.1. An integral theorem

Given a function f with period p, which maps real numbers onto real numbers then:

$$\frac{1}{p}\int_0^p\int_y^{y+b} f(x)\mathrm{d}x\mathrm{d}y = \frac{b}{p}\int_0^p f(x)\mathrm{d}x \tag{21}$$

where $b \leq p$. On the left hand side the integral $\int_y^{y+b} f(x)\mathrm{d}x$, represents the area under the curve over a length b, which will vary depending on y. The outer integral gives the sum of all such integrals as y going from 0 to p. Finally, the average area under the curve over a length b is calculated by dividing by p. It is proven below that this is equivalent to the right-hand side, which represents the proportion b/p of the area under the curve taken over one period. Firstly:

$$\int_y^{y+b} f(x)\mathrm{d}x = \int_0^b f(x+y)\mathrm{d}x \tag{22}$$

therefore:

$$\int_0^p\int_y^{y+b} f(x)\mathrm{d}x\mathrm{d}y = \int_0^p\int_0^b f(x+y)\mathrm{d}x\mathrm{d}y \tag{23}$$

Make the following substitutions: $x=s$ and $y=t-s$ (note that the determinant of the Jacobian of this transformation is one, see for example Fraleigh (1990, p. 840)) to give:

$$\int_0^p\int_0^b f(x+y)\mathrm{d}x\mathrm{d}y = \int_0^b\int_s^{s+p} f(t)\mathrm{d}t\mathrm{d}s \tag{24}$$

where $0 \leq s \leq b$ and $0 \leq t-s \leq p$. Now:

$$\int_s^{s+p} f(t)\mathrm{d}t = \int_0^p f(t)\mathrm{d}t + \int_s^{s+p} f(t)\mathrm{d}t - \int_0^s f(t)\mathrm{d}t \tag{25}$$

but:

$$\int_s^{s+p} f(t)\mathrm{d}t = \int_0^s f(t+p)\mathrm{d}t = \int_0^s f(t)\mathrm{d}t \tag{26}$$

because f has period p. Therefore Eq. (25) becomes:

$$\int_s^{s+p} f(t)\mathrm{d}t = \int_0^p f(t)\mathrm{d}t \tag{27}$$

Substituting Eq. (27) into Eq. (24) gives:

$$\int_0^p\int_0^b f(x+y)\mathrm{d}x\mathrm{d}y = \int_0^b\int_s^{s+p} f(t)\mathrm{d}t\mathrm{d}s$$

$$= \int_0^b\int_0^p f(t)\mathrm{d}t\mathrm{d}s = b\int_0^p f(t)\mathrm{d}t \tag{28}$$

By equating Eqs. (23), (24) and (28) and multiplying both sides by $1/p$, the theorem is proven.

Appendix A.2. Application to crystal fractions

In Fig. 11 three crystals are connected by an equilateral triangle and the percentage area of overlap between the three crystals and the triangle is required. However, in the model considered here, the orientations of the crystals are independently drawn from a uniform distribution on $[0, 2\pi]$ and are not fixed and parallel as shown in Fig. 11. Therefore in order to calculate the crystal fraction, we need to calculate the average area formed by the intersection of a crystal and the triangle. In Fig. 19 an arbitrary shape is shown with a fixed arc (i.e. represented by an angle of size b) subtended and the area of interest shaded. We wished to calculate the average area of the subtended region as θ goes from 0 to 2π. It is convenient to consider polar coordinates and therefore the boundary is defined by a function $r(\psi)$ where ψ is in the interval $[0, 2\pi]$. Note that any arbitrary shape considered in this way has a period of 2π (it may also have other periods). The area of the shaded region is (Fraleigh, 1990, pp. 588–589):

$$\frac{1}{2}\int_\theta^{\theta+b} r^2\mathrm{d}\psi$$

so that the average of all such areas for varying θ is:

$$\frac{1}{2\pi}\int_0^{2\pi}\left[\frac{1}{2}\int_\theta^{\theta+b} r^2\mathrm{d}\psi\right]\mathrm{d}\theta$$

which by the applying the above theorem is:

$$= \frac{b}{2\pi}\left[\frac{1}{2}\int_0^{2\pi} r^2\mathrm{d}\psi\right]$$

where the part in square brackets is the total area of the shape. In the case of three crystals (of equal area but not necessarily the same shape) connected by a triangle the sum of the subtended angles is π (from geometry) and therefore

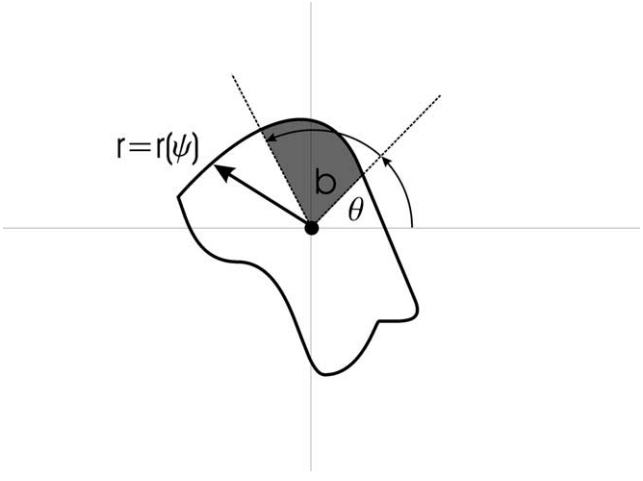

Fig. 19. An arbitrary shaped crystal is described by the polar function $r = r(\psi)$, where ψ is the angle in radians. The shaded region is the area subtended by an arc of b radians and θ is the angle between the arc and the x-axis. We wish to calculate the average area of the shaded region as θ varies uniformly from 0 to 2π.

the average overlap area between all three crystals and the triangle is half the area of a single crystal. A simple modification can be applied in the case of crystals of different areas.

References

Arbaret, L., Diot, H., Bouchez, J.-L., 1996. Shape fabrics of particles in low concentration suspension: 2D analogue experiments and application to tiling in magma. Journal of Structural Geology 18, 941–950.

Arzi, A.A., 1978. Critical phenomena in the rheology of partially melted rock. Tectonophysics 44, 173–184.

Blumenfeld, P., Bouchez, J.-L., 1988. Shear criteria in granite and migmatite deformed in the magmatic and solid states. Journal of Structural Geology 10, 361–372.

Bryon, D.N., Atherton, M.P., Hunter, R.H., 1994. The description of the primary textures of "Cordilleran" granitic rocks. Contributions to Mineralogy and Petrology 117, 66–75.

Correa-Gomes, L.C., Souza Filho, C.R., Martins, C.J.F.N., Oliveira, E.P., 2001. Development of symmetrical and asymmetrical fabrics in sheet-like igneous bodies: the role of magma flow and wall-rock displacements in theoretical and natural cases. Journal of Structural Geology 23, 1415–1428.

Den Tex, E., 1969. Origin of ultramafic rocks. Their tectonic setting and history. Tectonophysics 7, 247–262.

Devore, J.L., 1995. Probability and Statistics for Engineering and the Sciences. Duxbury Press, Pacific Grove. 743pp.

Fernandez, A., Febesse, J.L., Mezure, J.F., 1983. Theoretical and experimental study of fabrics developed by different shaped markers in two-dimensional simple shear. Bulletin de la Société géologique de France 25, 319–326.

Fleiss, J.L., 1981. Statistical Methods for Rates and Proportions. John Wiley and Sons, New York.

Fraleigh, 1990. Calculus with Analytical Geometry. Addison Wesley, Reading, Massachusets. 953pp.

Freeman, B., 1985. The motion of rigid ellipsoidal particles in slow flows. Tectonophysics 113, 163–183.

Ghosh, S.K., 1987. Measure of non-coaxiality. Journal of Structural Geology 9, 111–113.

Ghosh, S.K., Ramberg, H., 1976. Reorientation of inclusions by combination of pure shear and simple shear. Tectonophysics 34, 1–70.

Ildefonse, B., Sokoutis, D., Mancktelow, N.S., 1992a. Mechanical interactions between rigid particles in a deforming ductile matrix. Analogue experiments in simple shear flow. Journal of Structural Geology 14, 1253–1266.

Ildefonse, B., Launeau, P., Bouchez, J.-L., Fernandez, A., 1992b. Effect of mechanical interactions on the development of shape preferred orientations: a two-dimensional experimental approach. Journal of Structural Geology 14, 73–83.

Jeffery, G.B., 1922. The motion of ellipsoidal particles immersed in a viscous fluid. Proceedings of the Royal Society of London A 102, 201–211.

Jezek, J., Schulmann, K., Segeth, K., 1996. Fabric evolution of rigid inclusions during mixed coaxial and simple shear flows. Tectonophysics 257, 203–221.

Jezek, J., Saic, S., Segeth, K., Schulmann, K., 1999. Three-dimensional hydrodynamical modelling of viscous flow around a rotating ellipsoidal inclusion. Computers and Geosciences 25, 547–558.

Mandal, N., Samanta, S.K., Chakraborty, C., 2001. Numerical modeling of heterogeneous flow fields around rigid objects with special reference to particle paths, strain shadows and foliation drag. Tectonophysics 330, 177–194.

Means, W.D., Hobbs, B.E., Lister, G.S., Williams, P.F., 1980. Vorticity and non-coaxiality in progressive deformations. Journal of Structural Geology 2, 371–378.

Nicholas, A., 1992. Kinematics in magmatic rocks with special reference to gabbros. Journal of Petrology 33, 891–915.

Passchier, C.W., 1987. Stable positions of rigid objects in non-coaxial flow a study in vorticity analysis. Journal of Structural Geology 9, 679–690.

Passchier, C.W., 1997. The fabric attractor. Journal of Structural Geology 19, 113–127.

Passchier, C.W., Trouw, R.A.J., 1996. Microtectonics. Springer, Berlin.

Ramberg, H., 1975. Particle paths, displacements and progressive strain applicable to rocks. Tectonophysics 28, 1–37.

Samanta, K.S., Mandal, N., Chakraborty, C., 2003. Flow patterns around rigid inclusions in a multiple inclusion system under going bulk simple shear deformation. Journal of Structural Geology 25, 209–221.

Strogatz, S.H., 1994. Nonlinear Dynamics and Chaos with Applications to Physics, Biology, Chemistry, and Engineering. Perseus Books, Reading, Massachusetts.

Tikoff, B., Teyssier, C., 1994. Strain and fabric based on porphyroclast interaction. Journal of Structural Geology 16, 477–491.